J. Non-Newtonian Fluid Mech. 166 (2011) 554–565

Contents lists available at ScienceDirect

Journal of Non-Newtonian Fluid Mechanics

journal homepage: www.elsevier.com/locate/jnnfm

Floquet stability analysis of viscoelastic flow over a cylinder

David Richter, Eric S.G. Shaqfeh*, Gianluca Iaccarino

Stanford University, Stanford, CA 94305, United States

ARTICLE INFO

Article history:
Received 5 September 2010
Received in revised form 7 January 2011
Accepted 10 February 2011
Available online 19 February 2011

Keywords:
Viscoelastic simulation
Floquet stability analysis

ABSTRACT

A Floquet linear stability analysis has been performed on a viscoelastic cylinder wake. The FENE-P model is used to represent the non-Newtonian fluid, and the analysis is done using a modified version of an existing nonlinear code to compute the linearized initial value problem governing the growth of small perturbations in the wake. By measuring instability growth rates over a wide range of disturbance spanwise wavenumbers α, the effects of viscoelasticity were identified and compared directly to Newtonian results.

At a Reynolds number of 300, two unstable bands exist over the range $0 \leq \alpha \leq 10$ for Newtonian flow. For the low α band, associated with the "mode A" wake instability, a monotonic reduction in growth rates is found for increasing polymer extensibility L. For the high α band, associated with the "mode B" instability, first a rise, then a significant decrease to a stable state is found for the instability growth rates as L is increased from $L = 10$ to $L = 30$. The mechanism behind this stabilization of both mode A and mode B instabilities is due to the change of the base flow, rather than a direct effect of viscoelasticity on the perturbation.

1. Introduction

In our previous work we numerically investigated the effect of viscoelasticity on the flow over a circular cylinder by performing full nonlinear simulations [1]. For this canonical bluff body flow, many interesting modifications to the flow were found, particularly at Reynolds numbers lying in the regime of three-dimensional transition. It is well documented (see [2–4]) that the Newtonian transition from a two-dimensional, periodic wake to one that is three-dimensional goes through two secondary instability stages: the "mode A" instability at $Re \approx 190$ and the "mode B" instability at $Re \approx 260$. This mode A instability manifests itself as a spanwise row of alternating streamwise vortices in the near-wake, with a characteristic wavelength of roughly $4D$ (where D is the cylinder diameter) and a spatio-temporal symmetry where the streamwise vorticity changes sign on either side of a primary vortex. This has been found to exist as a subcritical instability (see [5]), explaining the hysteresis that is observed in experimental measurements of the critical Reynolds number where this transition takes place. The mode B instability appears also as alternating streamwise vortices in the near-wake, however with a smaller wavelength of about $1D$ and a symmetry which maintains the same sign of vorticity through a primary vortex. It also differs from the mode A instability in that it has been identified as a supercritical instability [5].

In the three-dimensional simulations of [1], the Reynolds number was set to be 300, well within the range where mode B instabilities would dominate the Newtonian wake. It is significant, therefore, that at high polymer extensibility L (in the FENE-P model) the wake is completely two-dimensional, without traces of streamwise vorticity. At intermediate values of L, streamwise vorticity remained, but in a state that was not easily identified as either mode A or mode B. The characteristic wavelength of vortical structures in this state appeared to be near that of the mode A instability, however they did not appear in the same spanwise-alternating form unique to the mode A instability.

These nonlinear results, along with the experimental work done by [6] illustrating similar stabilization behavior, are the motivation for the present linear stability analysis, whose goal is to better quantify the stabilizing effect that viscoelasticity has on the cylinder wake. For this purpose, a Floquet stability analysis is performed – a technique which has seen much success identifying the secondary instabilities that form from a two-dimensional, vortex shedding Newtonian wake. Noack and Eckelmann [7] were among the first to use Floquet analysis on the Newtonian cylinder wake, followed by Barkley and Henderson [4] a short time later. Barkley and Henderson [4] performed a detailed study over the entire range of $170 \leq Re \leq 300$ in order to pinpoint exactly the critical Reynolds numbers where the onset of the secondary mode A and mode B instabilities occurred. Their computed values of these critical Reynolds numbers matched very well quantitatively with the experiments of [3] and this success has prompted use of Floquet analysis for many other types of time-periodic wake

* Corresponding author.
E-mail address: esgs@stanford.edu (E.S.G. Shaqfeh).

0377-0257/$ – see front matter © 2011 Elsevier B.V. All rights reserved.
doi:10.1016/j.jnnfm.2011.02.005

flows such as square cylinders (see [8]) and confined cylinders (see [9]).

By utilizing the method presented by Robichaux et al. [8], growth rates for perturbations of the two-dimensional base flow in viscoelastic flow past a cylinder at various values of polymer extensibility L are computed and presented. Indeed elasticity reduces these growth rates in most cases, and the stabilization mechanisms are presented and discussed.

2. Problem formulation

2.1. Governing equations

As was done in [1], the FENE-P constitutive model is used to represent the presence of a dilute, homogeneous concentration of polymers within the flow. Thus the governing mass and momentum equations for the flow are given below in dimensionless form.

$$\frac{\partial u_j}{\partial x_j} = 0 \tag{1}$$

$$\frac{\partial u_i}{\partial t} + u_j \frac{\partial u_i}{\partial x_j} = -\frac{\partial p}{\partial x_i} + \frac{\beta}{Re}\frac{\partial^2 u_i}{\partial x_j \partial x_j} + \frac{1-\beta}{Re}\frac{1}{Wi}\frac{\partial \tau_{ij}^p}{\partial x_j} \tag{2}$$

Here, we have introduced a Reynolds number, $Re = \rho D U_\infty/(\mu_s + \mu_p)$, as a ratio of inertial to viscous forces; a Weissenberg number, $Wi = \lambda U_\infty/D$, as a ratio of the polymer relaxation time scale to the flow convective time scale; and a viscosity ratio, $\beta = \mu_s/(\mu_s + \mu_p)$, as the fraction of the total viscosity due to the solvent. Within these definitions, D refers to the cylinder diameter, U_∞ refers to the uniform upstream flow velocity, λ refers to the polymer relaxation time, μ_s refers to the solvent contribution to the total viscosity, and μ_p refers to the polymer contribution to the total viscosity.

In Eq. (2), the term involving τ_{ij}^p describes the force due to the additional polymeric stresses, and these are a function of the polymer conformation tensor c_{ij} and the polymer extensibility L:

$$\tau_{ij}^p = \frac{c_{ij}}{1 - (c_{kk}/L^2)} - \delta_{ij} \tag{3}$$

Finally, according to the FENE-P model, c_{ij} obeys the evolution equation

$$\frac{\partial c_{ij}}{\partial t} + u_k \frac{\partial c_{ij}}{\partial x_k} - c_{ik}\frac{\partial u_j}{\partial x_k} - c_{kj}\frac{\partial u_i}{\partial x_k} = -\frac{1}{Wi}\tau_{ij}^p \tag{4}$$

With this closed system of equations for velocity, pressure, polymer conformation, and polymer stress, the set of linearized equations required to perform the linear stability analysis can be obtained.

2.2. Linearized equations

By approximating the flow and polymer stress fields as a base flow plus a perturbation, it is possible to linearize equations (1)–(4). Capitalized characters will refer to base flow quantities, and primed characters will refer to fluctuations about the base state:

$$u_i = U_i + u_i' \tag{5}$$

$$p = P + p' \tag{6}$$

$$\tau_{ij}^p = T_{ij} + \tau_{ij}' \tag{7}$$

$$c_{ij} = C_{ij} + c_{ij}' \tag{8}$$

Substituting these definitions into Eqs. (1)–(4) and neglecting terms which are quadratic or higher in primed quantities yields a set of linearized FENE-P equations for the fluctuating quantities.

Mass conservation:

$$\frac{\partial u_j'}{\partial x_j} = 0 \tag{9}$$

Momentum conservation:

$$\frac{\partial u_i'}{\partial t} + U_j\frac{\partial u_i'}{\partial x_j} + u_j'\frac{\partial U_i}{\partial x_j} = -\frac{\partial p'}{\partial x_i} + \frac{1}{Re}\frac{\partial^2 u_i'}{\partial x_j \partial x_j} + \frac{1-\beta}{Re}\frac{1}{Wi}\frac{\partial \tau_{ij}'}{\partial x_j} \tag{10}$$

Linearized conformation tensor evolution equation:

$$\frac{\partial c_{ij}'}{\partial t} + U_k\frac{\partial c_{ij}'}{\partial x_k} + u_k'\frac{\partial C_{ij}}{\partial x_k} - C_{ik}\frac{\partial u_j'}{\partial x_k} - c_{ik}'\frac{\partial U_j}{\partial x_k} - C_{kj}\frac{\partial u_i'}{\partial x_k} - c_{kj}'\frac{\partial U_i}{\partial x_k} = -\frac{1}{Wi}\tau_{ij}' \tag{11}$$

Where the linearized polymer stress τ_{ij}' is given by:

$$\tau_{ij}' = \frac{L^2 C_{ij} c_{kk}'}{\left(C_{kk} - L^2\right)^2} + \frac{c_{ij}'}{1 - (C_{kk}/L^2)} \tag{12}$$

Because we are interested in the onset and growth of three-dimensional instabilities in the cylinder wake, a Fourier transform in the z (spanwise) direction is performed. By introducing a perturbation spanwise wavenumber α, we can approximate the perturbation field as a sum of Fourier modes in the spanwise direction:

$$u_i' = \int_{-\infty}^{\infty} \hat{u}_i e^{-i\alpha z}\, d\alpha \tag{13}$$

$$p' = \int_{-\infty}^{\infty} \hat{p} e^{-i\alpha z}\, d\alpha \tag{14}$$

$$c_{ij}' = \int_{-\infty}^{\infty} \hat{c}_{ij} e^{-i\alpha z}\, d\alpha \tag{15}$$

Since the equations governing the perturbations are linear, one can easily derive expressions for individual modes of $\hat{u}_i$, $\hat{p}$, and $\hat{c}_{ij}$ at a specified value of α from Eqs. (9)– (11), thus reducing the full three-dimensional problem to a coupled set of time dependent, purely two-dimensional (in x and y) equations with α as a parameter. The equations for the Fourier-transformed quantities, not shown here, are identical to Eqs. (9)–(11), with the exception that derivatives in the z-direction are replaced with $\partial/\partial z = -i\alpha$.

It should be noted that when performing a normal mode approximation such as that described above, the resulting Fourier coefficients can, in general, have both real and imaginary parts. For the current problem, however, this is not the case. Since we are only concerned with spanwise perturbations, and given the nature of the governing linearized equations (9)–(11), we find that the coefficients are always either purely real or purely imaginary. In particular, the phase of the spanwise velocity fluctuation w', as well as that of the components c_{13}' and c_{23}', is exactly out of phase with the remaining quantities. As a result, the coefficients $\hat{w}$, $\hat{c}_{13}$, and $\hat{c}_{23}$ are purely imaginary assuming all other quantities are purely real. By making the simple substitution $\tilde{w} = i\hat{w}$ (and similarly for $\tilde{c}_{13}$, and $\tilde{c}_{23}$), we guarantee that all coefficient values will be purely real-valued. Note, however, that for notational simplicity all coefficients will be referred to as "hat" quantities, despite actually solving for $\tilde{w}$, $\tilde{c}_{13}$, and $\tilde{c}_{23}$.

3. Numerical method

3.1. Base flow computations

Solving the full set of governing Eqs. (1)–(4) on a three-dimensional domain was the object of our previous work (see [1]),

and therefore the numerical details of the nonlinear solver will not be repeated here. It should suffice to say that the code is based on an unstructured finite-volume method, utilizing a fractional step method for handling the incompressibility constraint and a second order Crank–Nicholson scheme for time advancement.

In order to perform a Floquet stability analysis, a two-dimensional, time-periodic base flow past a cylinder must be computed for each chosen combination of Re, Wi, L, and β. These base flow simulations were done using the full nonlinear code, except that they were restricted to two-dimensional domains by ensuring all z-derivatives are exactly zero. Following the procedure of [4] and [8], these periodic base flow solutions providing U_i and C_{ij} were stored at 64 intervals over a single shedding period. They were then Fourier transformed in time, allowing for the Fourier series reconstruction of the solution at any simulation time and at any point on the computational mesh. It should be noted that in the previous studies of [4] and [8], 32 coefficients were adequate for accuracy in reconstructing U_i, but since in the present study C_{ij} must also be stored, and since the polymer conformation exhibits sharper features due to the low (artificial) diffusivity, 64 Fourier coefficients were required to maintain acceptable accuracy.

3.2. Modifications to nonlinear code

Aside from obtaining a base flow field, modifying the three-dimensional, fully nonlinear code was required to solve for the equations governing $\hat{u}_i$, $\hat{c}_{ij}$, and $\hat{p}$. This was done in a series of straightforward steps.

First, the code was altered such that it solves a linear set of transport equations (velocity and scalar transport equations) rather than a nonlinear set. For the momentum equation, the nonlinear convection term was originally discretized by first employing the divergence theorem over each grid volume, then storing a divergence-free advection velocity (obtained after solving the pressure Poisson equation during the previous time step) at the face of each finite-volume cell:

$$\int_\Omega u_j \frac{\partial u_i}{\partial x_j} \mathrm{d}V \approx \sum_f u_i U_f A_f \tag{16}$$

In Eq. (16), the index f refers to each face of a particular finite volume Ω, U_f refers to the advective face-normal velocity, and A_f refers to the face area. The advected velocity u_i is then computed at the face center using linear interpolation. In the present formulation, the advective face-normal velocity U_f was merely set to zero, $U_f = 0$, entirely eliminating the contribution from the nonlinear term. To then account for linear advection of and from the base flow ($u_j(\partial U_i/\partial x_j)$ and $U_j(\partial u_i/\partial x_j)$), these terms were treated explicitly in time using Green–Gauss reconstruction of the spatial gradients:

$$\frac{\partial \phi}{\partial x_i} \approx \frac{1}{V} \int_{\partial\Omega} \phi n_i \, \mathrm{d}A \approx \frac{1}{V} \sum_f \phi n_i A_f \tag{17}$$

where n_i is the face-normal unit vector and V is the cell volume.

For the $\hat{c}_{ij}$ evolution equations, a different procedure was used. Because $\hat{c}_{ij}$ is advected by U_i and not $\hat{u}_i$, the face-normal velocity U_f was set to be that of the base flow: $U_f = U_i n_i$ (where n_i is the volume face normal). This procedure thus maintained the semi-implicit QUICK (quadratic upwind interpolation for convective kinematics) discretization used in the original code for scalar advection (as opposed to setting $U_f = 0$ again), only with advection now being done by the reconstructed base flow. The remaining term, $u_k(\partial C_{ij}/\partial x_k)$, was then treated explicitly in time using expression (17).

Second, since the spanwise variation of the quantities of interest were parametrized by the wavenumber α, a minor modification of the pressure solver was required. The pressure solver used in the code is part of a fractional step method: first the momentum equation is solved using the pressure field from the previous time step, a Poisson system is solved for a pressure correction using the discrete continuity equation, and then the velocity is corrected to become discretely divergence-free.

As mentioned in the previous section, Eqs. (9)–(11) are identical to those governing $\hat{u}_i$, $\hat{c}_{ij}$, and $\hat{p}$, with the exception of z-derivatives being replaced with $\partial/\partial z = -i\alpha$, rendering the equations purely two-dimensional. Since the code is inherently three-dimensional, it solves for pressure via a full continuity equation, but computing the derivative $\partial\hat{w}/\partial z$ exactly equal to zero for the two-dimensional simulations:

$$\frac{\partial \hat{u}}{\partial x} + \frac{\partial \hat{v}}{\partial y} + \cancelto{0}{\frac{\partial \hat{w}}{\partial z}} = 0 \tag{18}$$

With the parameterization described above, however, the two-dimensional continuity equation is:

$$\frac{\partial \hat{u}}{\partial x} + \frac{\partial \hat{v}}{\partial y} = i\alpha w = \alpha \tilde{w} \tag{19}$$

Therefore, a "mass source" equal to $\alpha\tilde{w}$ was added into the Poisson system governing the pressure correction, accounting for spanwise variation which cannot be explicitly calculated (since all z-derivatives compute to exactly 0). This ensures a solution for $\hat{u}_i$ which discretely satisfies Eq. (19) at each time step.

3.3. Floquet analysis

Since the base flow solution for U_i, C_{ij}, and P are all periodic in time, Eqs. (9)–(11) are of Floquet type. After these equations are discretized, one can write the problem as an ordinary differential equation in the following way

$$\frac{\mathrm{d}\mathbf{q}}{\mathrm{d}t} = L(t)\mathbf{q} \tag{20}$$

where $\mathbf{q}$ is the solution vector containing $\hat{u}_i$, $\hat{p}$, and $\hat{c}_{ij}$ at each of the grid points, and $L(t)$ is a time-periodic, linear operator (with period T):

$$L(t) = L(t+T) \tag{21}$$

The general solution to a linear ODE of this form is:

$$\mathbf{q} = \mathbf{A}(t)\boldsymbol{q}_0 \tag{22}$$

where $\mathbf{A}$ is the $n \times n$ fundamental matrix containing n linearly independent solutions to (20), and $\mathbf{q}_0$ is the initial condition $\mathbf{q}(t=0)$. Note that for a steady base flow, $\mathbf{A}$ would consequently be steady, and a linear stability analysis would be concerned with the eigenvalues of the operator $\mathbf{A}$. For the present case, however, the Floquet theorem (see [10]) states that the T-periodic operator $\mathbf{A}(t)$ can be split into its periodic and exponentially varying parts:

$$\mathbf{A}(t) = \mathbf{P}(t)\exp(\mathbf{B}t) \tag{23}$$

where $\mathbf{P}(t)$ is T-periodic and $\mathbf{B}$ is a constant matrix. Furthermore, since the fundamental solution operator $\mathbf{A}(t)$ is periodic, integrating over a single period T would yield:

$$\mathbf{A}(t+T) = \mathbf{A}(t)\mathbf{C} \tag{24}$$

Here it is obvious that $\mathbf{C}$ contains the non-periodic evolution over a single period. From Eq. (23), we see that $\mathbf{C} = \exp(\mathbf{B}T)$.

Thus, the eigenvalues μ_n of $\mathbf{C}$ are known as the Floquet multipliers of the problem, governing the exponential rise or decay of the solution over each period. We note that the eigenvalues γ_n of $\mathbf{B}$ are

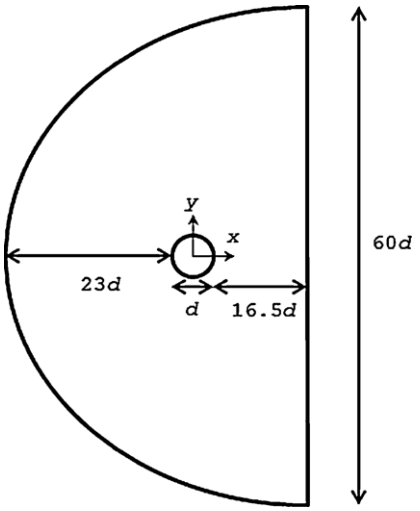

Fig. 1. Schematic of *xy* domain used for both base flow and Floquet calculations.

known as the Floquet exponents and are analogous to the eigenvalues of a typical steady (non-Floquet) linear stability problem. They are related to the Floquet multipliers by:

$$\mu_n = \exp(\gamma_n T) \tag{25}$$

In the Floquet stability analysis done by [4], the operator **C** was constructed and its largest eigenvalues were solved directly using a Krylov subspace method. In the present study, however, we take an approach identical to that of [8], who numerically solve the initial value problem of Eqs. (9)–(11) over a specified amount of time, and estimate the largest eigenvalue by measuring the growth or decay of fluctuation energy in the system. As done in [8], we define a perturbation energy integrated over the entire domain as:

$$E(t) = \int \sqrt{\hat{u}^2 + \hat{v}^2 + \hat{w}^2}\,dV \tag{26}$$

Then, the absolute value of the maximum eigenvalue can be approximated as:

$$|\mu_{max}| \approx \frac{E(t+T)}{E(t)} \tag{27}$$

This is equivalent to utilizing a power method to compute the largest magnitude eigenvalues of **C**, and therefore only provides information about the eigenvalue with the largest magnitude.

3.4. Boundary conditions

For the Floquet analysis, all simulations were performed on two-dimensional domains. Since the underlying code used is three-dimensional, meshes with only one cell in the spanwise (z) direction were used. Combining this type of mesh with periodic boundary conditions in the z-direction ensures that all $\partial/\partial z = 0$, thus resulting in purely two-dimensional calculations.

The *xy* domain and mesh used for both the base flow calculations and the Floquet analysis is identical to one used our previous work (see Figure 2 of [1]), and it is shown schematically in Fig. 1. There are only two outer boundaries on the domain: an inlet on the left, and one (vertical) outlet on the right. For the base flow calculations, boundary conditions were set to be exactly the same as done previously in [1], namely, a uniform velocity $U_\infty = [1, 0, 0]$ and equilibrium base flow polymer conformation $C_{ij,\infty} = \delta_{ij}$ along the entire inlet boundary (note $C_{ij,\infty} = \delta_{ij}$ only in the limit of $L \to \infty$, but in all cases here, this deviation from the true equilibrium conformation is negligible), and convective outlet conditions for both U_i and C_{ij}. At the cylinder wall, no-slip conditions are used for U_i and no-flux conditions are used for C_{ij} ($\partial C_{ij}/\partial n = 0$).

For the Floquet calculations, similar conditions are used for $\hat{u}_i$ and $\hat{c}_{ij}$. Both are set to zero along the entire inlet since there should be no perturbations upstream of the cylinder, and both also use convective outlet conditions. At the cylinder surface, no-slip conditions are applied to $\hat{u}_i$ and no-flux conditions are applied to $\hat{c}_{ij}$. Unlike the base flow computations, however, care must be taken in selecting initial conditions for the Floquet analysis. Since $\hat{u}_i$ and $\hat{c}_{ij}$ represent a spanwise perturbation amplitude, they are set equal to 1% of the base flow values everywhere in the domain:

$$\hat{u}_i(t=0) = 0.01 U_i(t=0) \tag{28}$$

$$\hat{c}_{ij}(t=0) = 0.01 C_{ij}(t=0) \tag{29}$$

It is this initial disturbance whose energy will be tracked and used to compute maximum instability growth rates.

One final note must be made about the pressure disturbance $\hat{p}$. In typical incompressible simulations, the reference value (and thus the absolute value) of the pressure p is unimportant since it only appears inside a gradient in the momentum equations. For the equations governing $\hat{u}_i$, $\hat{c}_{ij}$, and $\hat{p}$ (Eqs. (9)–(11)), however, this is not the case. Since all gradients in the z direction are set to $-i\alpha$, pressure appears explicitly in the $\hat{w}$ momentum equation:

$$\frac{\partial \hat{w}}{\partial t} + \hat{u}_j \frac{\partial \hat{w}}{\partial x_j} = i\alpha\hat{p} + \frac{\beta}{Re}\frac{\partial^2 \hat{w}}{\partial x_j \partial x_j} + \frac{1-\beta}{Re}\frac{1}{Wi}\frac{\partial \hat{\tau}_{3j}^p}{\partial x_j} \tag{30}$$

Therefore its value becomes important and $\hat{p}$ requires a Dirichlet boundary condition to set the reference pressure. As with $\hat{u}_i$ and $\hat{c}_{ij}$, there should be no perturbations in any of the flow quantities upstream, so $\hat{p}$ was set to zero at the single node lying where the front stagnation point streamline meets the domain inlet:

$$\hat{p}(x = -23D, y = 0) = 0 \tag{31}$$

4. Results

4.1. Comparison of Newtonian calculations

Before performing the Floquet stability analysis for the viscoelastic case, Newtonian growth rate calculations were done to compare to the existing work of [4]. Fig. 2 shows the absolute value of the largest magnitude Floquet multiplier, $|\mu|$, versus the

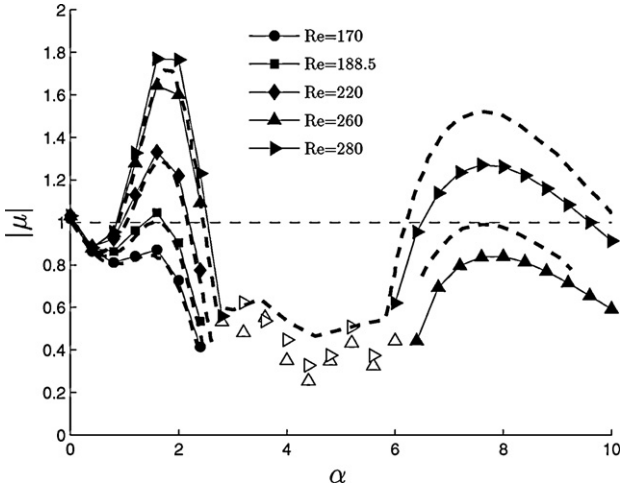

Fig. 2. Computed values of the largest magnitude Floquet multiplier $|\mu|$ versus spanwise wavenumber α for purely Newtonian flow at different Reynolds numbers. These are compared to the results of [4] (thick dashed lines). Hollow symbols indicate complex-valued Floquet multipliers.

spanwise wavenumber of the disturbance, α, at several different Reynolds numbers. The values obtained by [4] have been digitized and plotted on top of the current results as thick dashed curves. The authors of [4] found two unstable bands of spanwise wavenumber as the Reynolds number is increased. The first band occurs at $Re = 188.5$, and has a peak growth rate at a spanwise wavenumber of $\alpha \approx 1.6$. This is in very close quantitative agreement with experimental measurements of the wavelength of the mode A instability that forms at nearly the same Reynolds number (see [3]). As the Reynolds number is increased, Barkley and Henderson [4] then find a second band of unstable wavenumbers which develops at $Re = 259$. This band is centered about a spanwise wavenumber of $\alpha \approx 7.6$, which again shows good agreement with experimental measurements of the mode B instability wavelength.

Using our present technique, we find agreement within 5% for the growth rates at α encompassing the first unstable band. For the wavenumber band at higher α, however, differences of up to 16% are found in the growth rate. The cause of this discrepancy was investigated, and it was found to be a result of a difference in domain size between the current study and that used in [4], and not due to time step or grid resolution. When reducing the size of the current domain to match that of the eigenvalue calculations of [4] (note they use different domain sizes for base flow calculations and eigenvalue calculations), errors are reduced to within 5%. Furthermore, an additional calculation was performed on the square cylinder of [8], whose method for computing eigenvalues we have adopted, and obtained Floquet multiplier values which are nearly identical. Ultimately, we are not concerned with the values of the growth rates themselves, but only whether or not the flow has been stabilized or destabilized by the presence of viscoelasticity.

Before moving onto viscoelastic calculations, one more note must be made. Because we are measuring the instability growth rate using expression (27) and not actually computing the eigenvalues of the operator **C**, only the absolute value of the largest eigenvalue can be found – no information about the complex angle is available. It is this fact that caused [8] to mistakenly identify what they measured as a third unstable, subharmonic mode in the wake of a square cylinder. As shown in detail by [11], measurements of the growth rate by Eq. (27) implicitly assumes the largest magnitude multiplier μ is purely real, while the actual Floquet multiplier (calculated directly from the eigenvalues) exists as a pair of complex-conjugate values in this third unstable band. The result is what [11] calls a quasiperiodic mode instead of the unstable subharmonic mode found by [8], which manifests itself as a standing or traveling wave. This mode introduces a new frequency into the system due to the complex part of the eigenvalue, and as a result, plots of $|\mu|$ computed with (27) versus time exhibit oscillations about the actual value of $|\mu|$ computed directly from its eigenvalues. This is illustrated in Fig. 3, which shows plots of $|\mu|$ versus time for $Re = 300$ and two values of α. For $\alpha = 1.6$, $|\mu|$ clearly levels to a constant value of $|\mu| \approx 1.87$. For $\alpha = 4.0$, however, the signal clearly has additional frequency input likely due to the presence of a complex-conjugate pair of eigenvalues, and eventually approaches a state which oscillates (and does not decay further) around the value $|\mu| \approx 0.5$. From [4] we see that $\alpha = 4.0$ does in fact lie within a region of complex-conjugate pair multipliers, indicated by hollow circles in their Figure 7 (not reproduced here in the digitized data included in Fig. 2).

Therefore, by observing whether or not the signal of $|\mu|$ versus time has an oscillatory component which remains indefinitely, it is possible to at least qualitatively predict whether or not the multiplier with the largest magnitude is purely real. Using this observation for at least 20 shedding periods, plots of growth rates included in this paper will use hollow symbols to indicate what is likely a complex eigenvalue. While using this method it is still impossible to determine the actual values of the real and complex parts of each multiplier, the present approach serves the purpose of determining stability characteristics of viscoelastic flow around a cylinder.

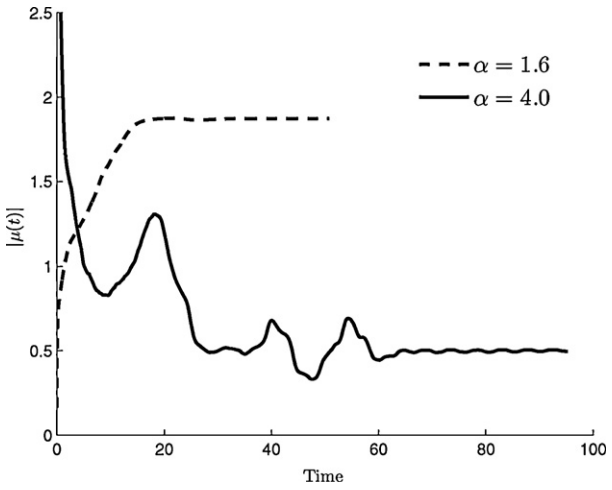

Fig. 3. Plot of growth rate $|\mu|$ versus time for two different spanwise wavenumbers: $\alpha = 1.6$ and $\alpha = 4.0$. $\alpha = 1.6$ lies in a range with the largest eigenvalue being purely real, while $\alpha = 4.0$ lies in a range where largest magnitude eigenvalue is a pair of complex-conjugate values, resulting in an oscillatory signal. Both plots are for $Re = 300$.

4.2. Viscoelastic results

After confirming the predictive capability of our method on the stability of two-dimensional, periodic wakes for Newtonian flow, the same analysis was done for the viscoelastic case. Plots of the computed growth rates versus spanwise wavenumber α are shown for various values of the polymer extensibility L in Fig. 4 at $Re = 300$, $Wi = 10$, and $\beta = 0.9$.

As with the Newtonian case, a grid refinement test was done to ensure that the growth rates obtained are grid independent for the viscoelastic results. By repeating the same calculations for a refined mesh at a single value of α in each unstable band ($\alpha = 1.6$ and $\alpha = 7.6$), the grid independence of each viscoelastic case was established. Over all values of L, the largest change in growth rate due to grid refinement was 6.5%. As mentioned above, this is certainly adequate for the purposes of determining the degree of stabilization due to viscoelasticity.

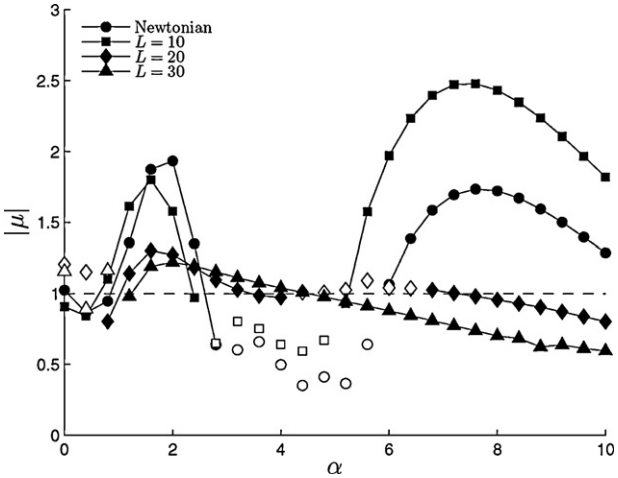

Fig. 4. Computed values of maximum instability growth rate $|\mu|$ versus spanwise wavenumber α for viscoelastic flow at $Re = 300$ and increasing values of the polymer extensibility L. All simulations performed with $Wi = 10$ and $\beta = 0.9$. Hollow symbols indicate complex-valued multipliers.

Focusing for the moment only on the low wavenumber unstable band ($0 \leq \alpha \leq 3$), increases in the polymer extensibility clearly result in a monotonic decrease in the maximum growth rate. From Newtonian flow to viscoelastic flow with $L = 30$, the peak growth rate in the mode A unstable band decreases by 37%. Furthermore, the range of unstable α is widened, as well as shifted slightly towards larger α.

For the higher band of unstable α ($5 \leq \alpha \leq 10$), there is instead a non-monotonic reduction in the instability growth rates. For $L = 10$, there is actually a substantial increase in the growth rate of perturbations (43% increase in the peak value), along with a widening of the wavenumber range over which instability growth occurs. As L is increased beyond this value, however, there is a near total suppression of instability growth. In fact, one could argue that for $L = 20$ and $L = 30$, the existence of a mode B "band" is eliminated completely (especially for $L = 30$). Thus, as L is increased beyond $L = 10$ a single growth rate curve emerges, whose only unstable region exists near wavelengths associated with the mode A instability, and whose growth rates smoothly decrease as the wavenumber α is increased.

4.3. Comparison to nonlinear results

In [1] it was shown using nonlinear, three-dimensional simulations that increasing L in cylinder flow at $Re = 300$ could eventually result in a total elimination of three-dimensionality in the wake. For the Newtonian case, a clear mode B structure of alternating streamwise vortices immediately behind the cylinder was found. When viscoelasticity was introduced at a polymer extensibility of $L = 10$, streamwise vorticity remained present in the wake, but in a weakened and altered state. Instantaneous snapshots of the streamwise vorticity ($\omega_x \pm 0.5$) for these simulations, plus that for $L = 20$ are shown in Fig. 5 (same as in Figure 12 of [1] but from a different angle). The orientation of the figure is looking directly downstream through the cylinder, such that the spanwise vortical structures present in the wake are clearly visible. From the stability results presented above, one would initially expect to see a wake dominated by mode B structures at $L = 10$, much like Newtonian flow at the same Reynolds number, since the growth rates in this range of α have increased dramatically from their Newtonian counterpart. Categorizing the state found from nonlinear simulations at $L = 10$ as either exhibiting mode A or mode B instabilities, however, is not straightforward. It was suggested in [1] that the wake was possibly being reverted back to a state resembling the mode A instability based solely on the wavelength of the dominant structures behind the cylinder (this wavelength of $\lambda_z \approx 3.5$ can clearly be seen in Fig. 5(b)). However, the present results indicate that the state of the wake at $L = 10$ is the culmination of nonlinear processes rather than a direct realization of an eigenmode of the linear stability analysis. In Fig. 5(b), there is evidence in the region immediately behind the cylinder of streamwise vorticity growth which may have a characteristic wavelength in the high-α unstable region of Fig. 4, but the overall structure is clearly not just a representation of the critical Floquet mode.

For $L = 20$, the case is slightly different. From Fig. 4, we see that there is again exponential growth of perturbations lying in one of two unstable regions, still somewhat analogous to the mode A and mode B bands of the Newtonian case: $1.0 \lesssim \alpha \lesssim 3.4$ or $5.2 \lesssim \alpha \lesssim 7.2$. However, the growth of the high-α modes is significantly smaller than those from the low-α band, so based on linear theory alone, one would now expect to observe a state devoid of mode B structures (i.e. one resembling the mode A wake), despite still being at a Reynolds number of 300. As opposed to the $L = 10$ case, this would now seem to reinforce the suggestion from [1] that viscoelasticity is merely delaying the Newtonian modes of transition. By examining the nonlinear solution at the same value of L (seen in Fig. 5(c)), the wake does in fact take a form resembling that of the mode A instability. However, the wavelength that appears in the nonlinear simulation (roughly $\lambda_z \approx 1.6D$) is higher than that predicted by the Floquet analysis, again suggesting nonlinear growth of spanwise perturbations beyond the linear regime.

One important issue mentioned in [4] that should be noted here is the applicability of linear stability analysis to the appearance of the mode B instability. The base state chosen for the linear stability analysis was the two-dimensional, vortex shedding wake, therefore the growth rates found are for perturbations growing from this state. It is well-known experimentally (see [3,12]) that the mode A instability precedes the mode B instability, and thus the mode B instability is growing from a state already exhibiting the mode A instability – not the two-dimensional base state. Despite this, Barkley and Henderson [4] found relatively good qualitative and quantitative agreement to experiments of the mode B critical Reynolds number, as well as the wavelength and symmetry of the resulting modes. When considering this for the present results, the effect may be amplified due to the additional nonlinearity of the viscoelastic contribution – a fact illustrated by the differences between the linear and nonlinear calculations at $L = 10$.

5. Mechanism discussion

5.1. Mode A stabilization mechanism

As pointed out in the previous section, Fig. 4 shows a monotonic decrease in the perturbation growth rates with increasing polymer extensibility L over the unstable wavenumber band associated with the mode A (long wavelength) instability. The mechanism responsible for this stabilization will be discussed further.

For Newtonian flow past a cylinder, it has been argued that the nonlinear mode A instability is a direct result of an "elliptic" instability of the vortex core (see [3,13,14]), and its wavelength therefore scales on the size of the primary spanwise vortices. This elliptic instability is an amplification of inertial waves in a flow with elliptical streamlines, and it is physically due to the alignment and resonance of traveling disturbance waves with the strain field. The existence of such instabilities has been shown analytically to exist for unbound elliptical flows (see [15–17]) and furthermore [18] showed that these instabilities can still exist in nearly the same form but within bounded domains, such as inside a primary spanwise vortex. For the cylinder wake at high enough Reynolds number, the argument given by [13] is that during their development, elliptic instabilities begin to form within the primary vortex cores near the base of the cylinder. These instabilities are then advected downstream while being amplified in the high strain rate region between primary vortex cores and eventually give rise to the mode A instability. Rough estimates of the symmetry and spanwise wavenumber of these elliptic instabilities compares well with those of the mode A instability, and patterns of the instability within a developing vortex appears qualitatively similar to growing modes of the elliptic instability.

Consistent with this mode A mechanism is a recent study by [19] which investigates the spatial origins of the mode A and mode B instabilities by determining the locations in the flow where a perturbation force-velocity feedback is maximized. This study corroborates the Floquet analysis done on successively reduced domains by [20] and shows that the mode A instability is formed in a relatively small region very close to the back of the cylinder (within $1.5D$ of the rear stagnation point). Therefore, not only does this support the elliptic instability mechanism, but it also provides a location to begin looking for the stabilizing cause of viscoelasticity.

Fig. 6 shows contours of perturbation energy normalized by the total integrated energy for increasing values of L at $Re = 300$,

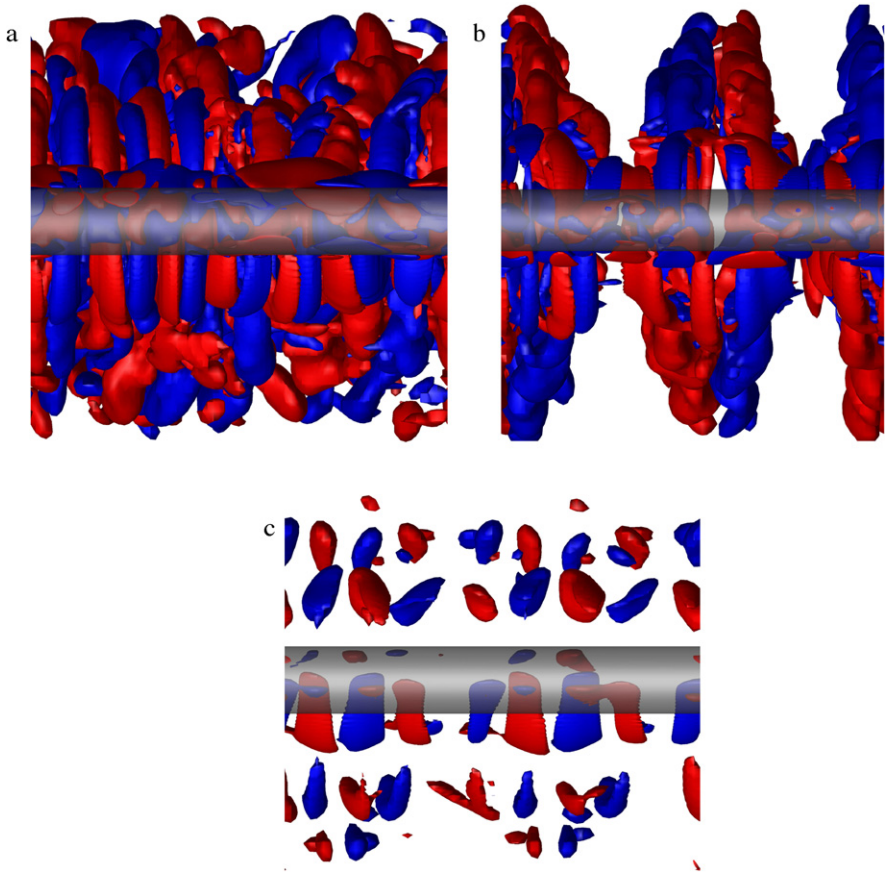

Fig. 5. Instantaneous snapshots of streamwise vorticity ($\omega_x \pm 0.5$) in the nonlinear wake for $Re = 300$. Orientation is looking in the downstream direction, through the cylinder at the y–z plane. Results are for (a) Newtonian flow; (b) $Wi = 10$, $L = 10$, $\beta = 0.9$; (c) $Wi = 10$, $L = 20$, $\beta = 0.9$.

$Wi = 10$ and $\beta = 0.9$ (for the viscoelastic cases) and with a spanwise wavenumber of $\alpha = 1.6$. From the figure it is obvious that the overall amount of perturbation energy has decreased with increasing L. In agreement with the argument described above, perturbation energy clearly begins to form within the developing primary vortex (seen on the bottom side of the cylinder in each figure) and is then amplified in the region between the developing vortex and its predecessor. For $L = 10$, there are not many noticeable differences in the distribution or amplitude of perturbation energy throughout the wake, however for $L = 20$, the amplitudes of perturbation energy are reduced dramatically. This is entirely consistent with the decrease in growth rates shown in Fig. 4, however it does not yet lead to an explanation of exactly how viscoelasticity is responsible for such a reduction in perturbation growth. To help answer this question, terms from the overall budget of perturbation energy were computed and integrated over the entire domain. A new perturbation energy is defined (as opposed to that in Eq. (26)):

$$\hat{E} = \frac{1}{2}\hat{u}_i\hat{u}_i^* \tag{32}$$

An evolution equation for $\hat{E}$ can then be easily obtained by multiplying the equation for $\hat{u}_i$ (Eq. (10) with u' replaced by $\hat{u}_i$ and z-derivatives replaced by $-i\alpha$) by $\hat{u}_i^*$ and averaging this with $\hat{u}_i$ multiplied by the conjugate of the same equation. This results in a balance of terms for the time rate of change of total perturbation energy (these equations also follow $\partial/\partial z = -i\alpha$):

$$\frac{\partial E}{\partial t} = BCV + CV + PR + NS + VS \tag{33}$$

In this budget, the different terms correspond to: *BCV* is convection of the energy by the base flow:

$$BCV = U_j\frac{\partial \hat{E}}{\partial x_j} \tag{34}$$

CV is the production of perturbation energy by interaction with the base flow:

$$CV = \frac{1}{2}\left[\hat{u}_i\hat{u}_j^*\frac{\partial U_i}{\partial x_j} + \hat{u}_i^*\hat{u}_j\frac{\partial U_i}{\partial x_j}\right] \tag{35}$$

PR is the pressure term:

$$PR = \frac{1}{2}\left[\hat{u}_i^*\frac{\partial \hat{p}}{\partial x_i} + \hat{u}_i\frac{\partial \hat{p}^*}{\partial x_i}\right] \tag{36}$$

NS is the dissipation due to Newtonian viscosity:

$$NS = \frac{1}{2}\frac{\beta}{Re}\left[\hat{u}_i^*\frac{\partial^2\hat{u}_i}{\partial x_j^2} + \hat{u}_i\frac{\partial^2\hat{u}_i^*}{\partial x_j^2}\right] \tag{37}$$

And finally *VS* is the contribution of viscoelasticity to the total perturbation energy:

$$VS = \frac{1}{2}\frac{(1-\beta)}{Re}\frac{1}{Wi}\left[\hat{u}_i^*\frac{\partial\hat{\tau}_{ij}}{\partial x_j} + \hat{u}_i\frac{\partial\hat{\tau}_{ij}^*}{\partial x_j}\right] \tag{38}$$

After integrating these values over the entire domain at each time step, plots of these total quantities versus time were created in order to observe the relative balance of the terms at each stage within a shedding period. Fig. 7 presents plots of these quantities for Newtonian flow, $L = 10$, and $L = 20$ (again with $Wi = 10$ and $\beta = 0.9$) over two periods, normalized by the total instantaneous energy at

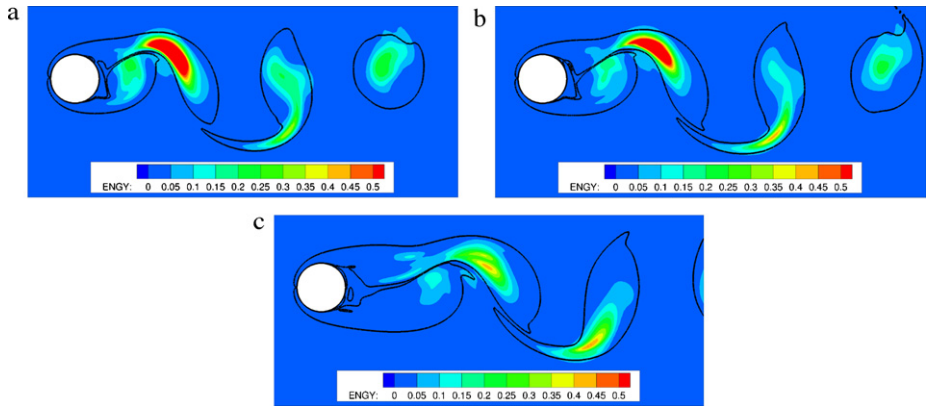

Fig. 6. Contours of perturbation energy given by Eq. (32), scaled by the total integrated energy at the current time. Lines of constant base flow vorticity are also shown with solid black lines for values of $\Omega_z = \pm 0.5$. Results are for (a) Newtonian flow; (b) $L = 10$; and (c) $L = 20$. All three calculations are for $Re = 300$, and all viscoelastic calculations are for $Wi = 10$ and $\beta = 0.9$.

each time. As in Fig. 6, there are not many differences between the Newtonian and the $L = 10$ case. In both cases, the base flow convection (BCV) is nearly zero, and the pressure term (PR) contributes very little to the overall energy budget. For $L = 10$, the viscoelastic term (VS) appears as a sink, however a very weak one. The energy budget therefore results for both of these cases primarily in a balance between production (CV) and dissipation (NS) with production slightly greater, leading to the growth of perturbation energy and the overall instability. Our interest, however, is in the $L = 20$ case, where significant reductions in instability growth rates and perturbation energy have already been observed. In Fig. 7(c) we see that once again the base flow convection and the pressure term contribute very little to the overall balance of the perturbation energy. Furthermore, the viscoelastic term again appears as a very weak sink, leaving the primary balance to lie between the production and dissipation. The main difference in the $L = 20$ case, however, is in the decreased production seen over the entire shedding cycle. While the magnitude of the dissipation is only slightly decreased from that of the Newtonian case, the significantly diminished production is what is responsible for the reduction in perturbation growth rate. It therefore appears that rather than acting as a direct sink of perturbation energy in the balance, viscoelasticity instead reduces the effectiveness of the perturbations from extracting energy out of the underlying base flow.

From Fig. 6 an explanation for this indirect stabilization can be extracted. Focusing only on the structure of the underlying base

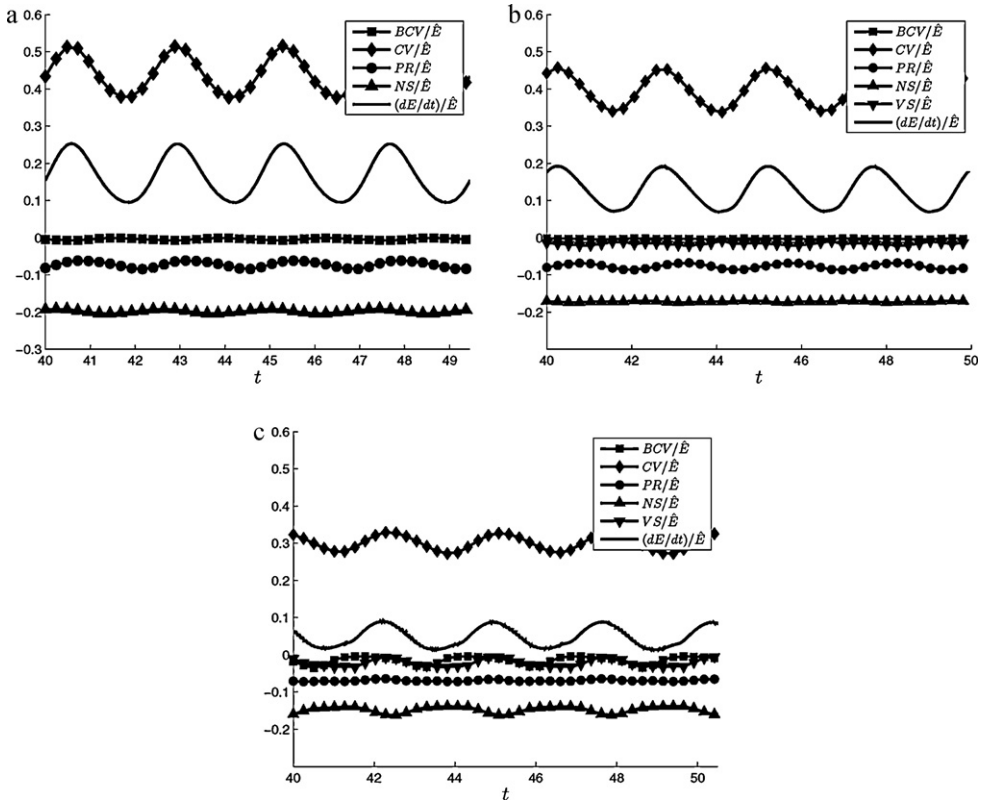

Fig. 7. Time signals of each of the components of the energy balance over two base flow shedding periods for spanwise wavenumber of $\alpha = 1.6$ (see text for explanation of the symbols). Energy components scaled by total energy at current time. (a) Newtonian case; (b) $L = 10$ case; (c) $L = 20$ case. All three calculations are for $Re = 300$, and all viscoelastic calculations are for $Wi = 10$ and $\beta = 0.9$.

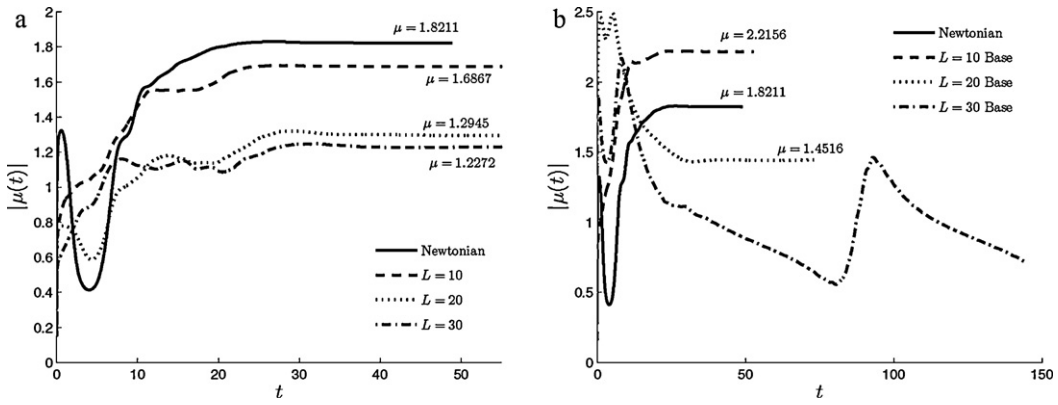

Fig. 8. Plots of Floquet multiplier $|\mu|$ versus time for the (a) full viscoelastic case; (b) Newtonian Floquet analysis with viscoelastic base flows corresponding to $L = 10$, $L = 20$, and $L = 30$. Calculations for spanwise wavenumber $\alpha = 1.6$.

flow (given in terms of the spanwise vorticity with solid black lines), it is clear that increasing viscoelasticity can significantly alter the primary vortex structure of the base flow, perhaps into a state which is less susceptible to perturbation energy growth and thus more stable to three-dimensional disturbances. The differences between the Newtonian and $L = 10$ base flows are again very small, while for the $L = 20$ case the wake structure is more elongated and the primary vortex formation is further from the rear of the cylinder.

To test the hypothesis that it is this base flow modification that stabilizes the flow, a Newtonian Floquet analysis was performed while using the viscoelastic base flows. In this case, viscoelasticity plays no role whatsoever, and any differences in the growth rates would be a result of the change in base flow. For $\alpha = 1.6$, results of this test (in terms of the Floquet multiplier $|\mu|$ versus time) are compared to the full viscoelastic computations in Fig. 8. As mentioned before, the full calculations result in a monotonic decrease in the Floquet multiplier as L is increased. This is seen clearly in Fig. 8(a). For the Newtonian calculation on the varying base flows, however, the story is much different. At $L = 10$, the multiplier actually levels off to a value 20% higher than the Newtonian case. Increasing L beyond this value however leads to a reduction in $|\mu|$ for $L = 20$, then to a time signal indicative of a complex multiplier (oscillatory $|\mu|$ versus time signal) for $L = 30$, whose magnitude is further diminished. Even without the presence of the viscoelastic term in the perturbation energy budget, the instability growth rates can clearly still be reduced by changing the base flow. For $L = 10$, the increase in $|\mu|$ is somewhat surprising, but is consistent with the fact that the base flow has not changed significantly. The small changes that do exist are such that production is slightly increased for this case. For $L = 20$ and even more so at $L = 30$, the base flow becomes so altered that its state is much less susceptible to three-dimensional disturbances. This is similar to the findings of Kumar and Homsy [21], who performed a three-dimensional stability analysis of a two-dimensional, viscoelastic shear layer which has already undergone a roll-up instability. After illustrating that viscoelasticity actually destabilizes for low elasticity, they proposed that at higher values of L, viscoelasticity can alter the process of two-dimensional roll-up to the point that the final state is much less sensitive to three-dimensional perturbations.

As mentioned at the beginning of this section, the mode A instability has been associated with an elliptic instability in the developing primary vortex core, and clearly this process is altered by the presence of viscoelasticity in the base flow. Therefore, to determine why viscoelasticity is behaving as a perturbation energy sink (albeit a weak one), the results of analytical work done by Lagnado and Simmen [22] and Haj-Hariri and Homsy [23] are applied to the present case. Lagnado and Simmen [22] conducted an analytical study on the effects of viscoelasticity on the elliptic instability of vortices and found a destabilizing influence which dominates for instability wavevectors nearly perpendicular to the vortex axis. Independently, Haj-Hariri and Homsy [23] found very

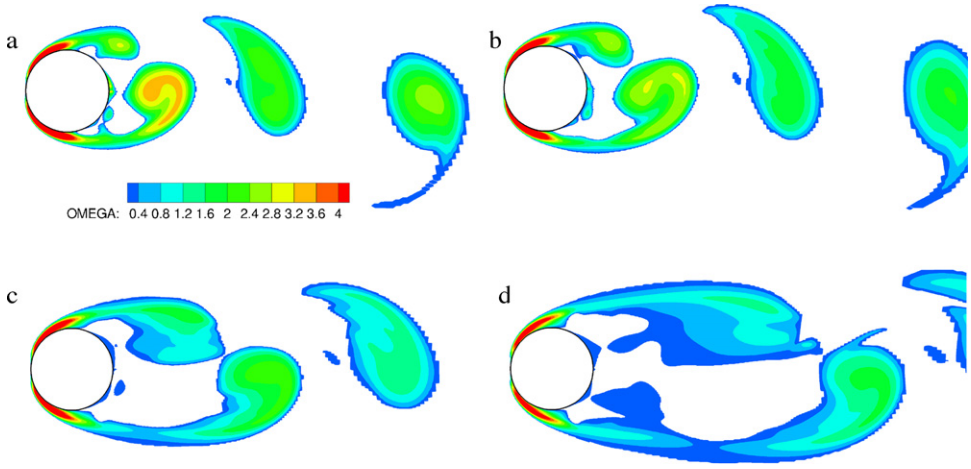

Fig. 9. Contour plots of rotation rate, measured as $\Omega = \sqrt{\gamma^2 - \epsilon^2}$ where γ is the half the local vorticity and ϵ is the maximum strain rate in linear elliptical flow. Note that contours are only drawn where flow is elliptic (i.e. $|\gamma| > |\epsilon|$). Plots illustrate increasing polymer extensibility: (a) Newtonian, (b) $L = 10$, (c) $L = 20$, and (d) $L = 30$, where $Re = 300$, $Wi = 10$, and $\beta = 0.9$.

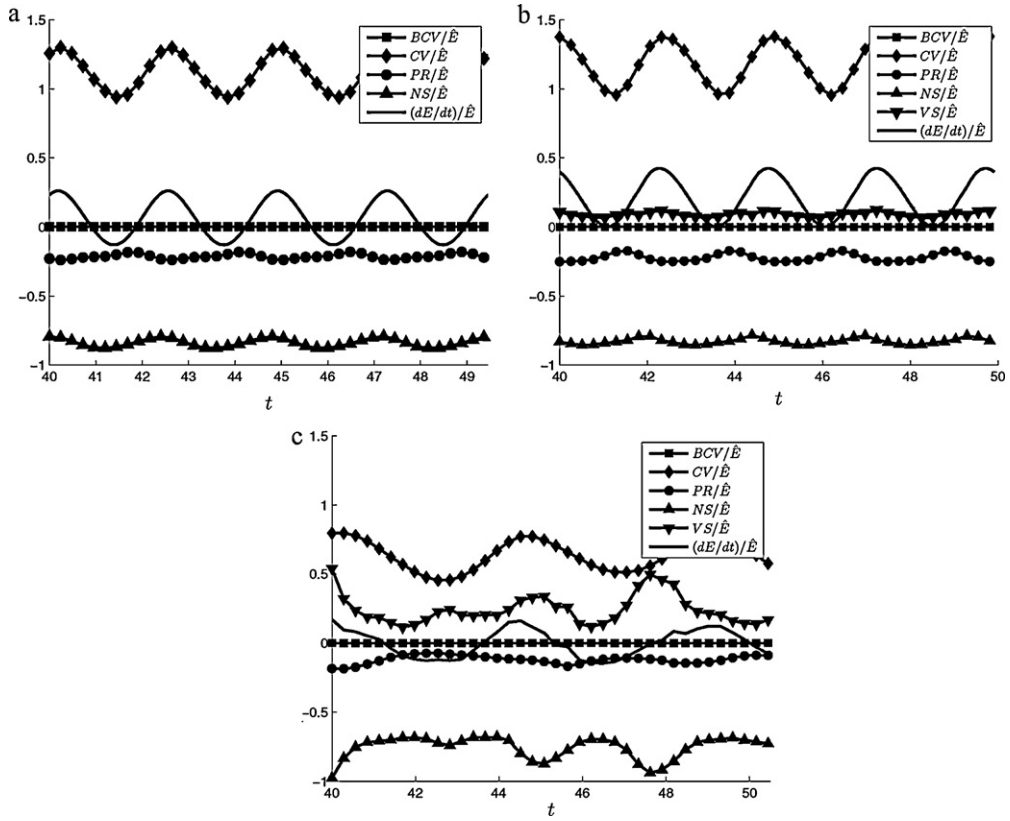

Fig. 10. Time signals of each of the components of the energy balance over two base flow shedding periods for spanwise wavenumber of $\alpha = 7.6$ (see text for explanation of the symbols). Energy components scaled by total energy at current time. (a) Newtonian case; (b) $L = 10$ case; (c) $L = 20$ case. All three calculations are for $Re = 300$, and all viscoelastic calculations are for $Wi = 10$ and $\beta = 0.9$.

similar results and elaborated on this new mode of instability which exists for the vanishing spanwise component of the instability wavevector. Both of these findings, unfortunately, are not directly applicable to the present case since we have restricted the perturbation wavevector to lie exactly in the spanwise direction, and thus it does not have a vanishing spanwise component for finite α. As a result, comparisons of their findings can only be made at near-zero values of the angle θ between the rotating wavevector and the axis of the elliptic vortex, and only [23] provides details of instability growth rates at such angles. Comparing the stability diagrams of [23] for both the inviscid (their Figure 1) and viscoelastic (their Figure 3) cases, we see that at low values of θ there is indeed a small but finite amount of stabilization in the growth rates over all values of ellipse eccentricity. Because much of the focus of their work was on the new mode of in-plane instability, no discussion was made of this stabilization at low values of θ, but it suffices to say that this stabilization is clearly consistent with our present results. However, as argued above, this is only a minor effect since it does not in any way account for the reduction of perturbation energy production – it only uncovers why viscoelasticity can extract perturbation energy from the system.

What is more important is determining what causes these altered base flows to be more or less stable to three-dimensional instabilities. By looking at certain kinematic quantities (vorticity, strain rate, etc.) inside the primary vortices, one can qualitatively anticipate the change in stability of various base flows. Although it was stated above that the findings of [22] and [23] were not directly applicable to the current study, in each of these investigations the instability growth rates were found to scale proportionally with a measure of vortex rotation rate ($\Omega = \sqrt{\gamma^2 - \epsilon^2}$, where γ is half

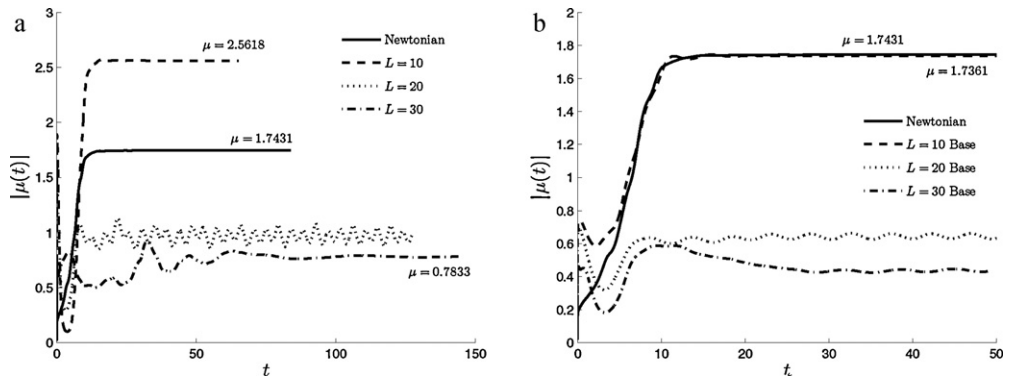

Fig. 11. Plots of Floquet multiplier $|\mu|$ versus time for the (a) full viscoelastic case; (b) Newtonian Floquet analysis with viscoelastic base flows corresponding to $L = 10$, $L = 20$, and $L = 30$. Calculations for spanwise wavenumber $\alpha = 7.6$.

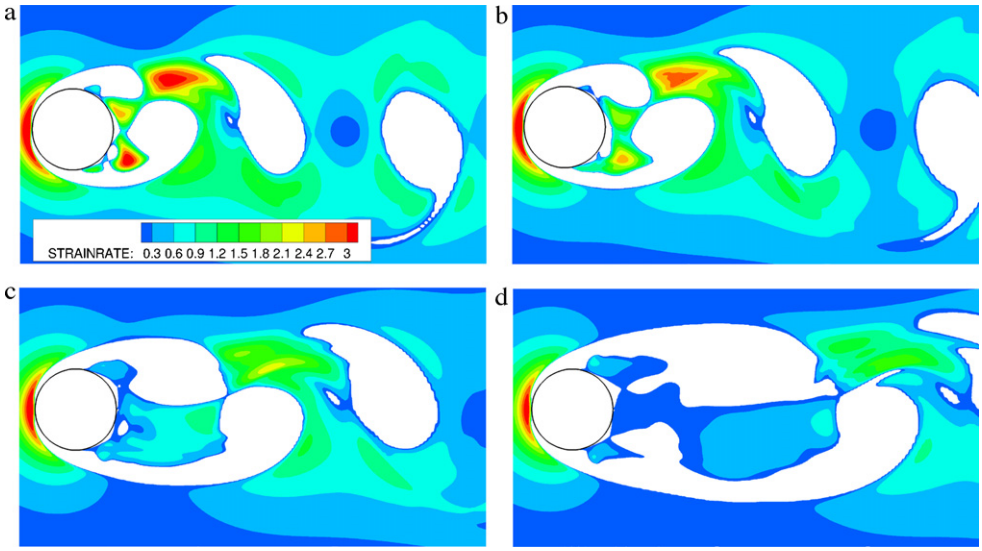

Fig. 12. Contour plots of principal strain rate, measured along the principal axes in hyperbolic. Note that contours are only drawn where flow is elliptic (i.e. $|\epsilon| > |\gamma|$). Plots illustrate increasing polymer extensibility: (a) Newtonian, (b) $L = 10$, (c) $L = 20$, and (d) $L = 30$, where $Re = 300$, $Wi = 10$, and $\beta = 0.9$.

the vorticity and ϵ is the maximum strain rate in a linear elliptical flow). This scaling of growth rate with elliptic rotation rate is consistent with the Newtonian analyses as well [15–17], and shows that an overall reduction of vorticity or rotation within the developing primary vortex core would correspondingly reduce the growth of three-dimensional instabilities. This is indeed the case, as increasing polymer extensibility is observed to significantly reduce the magnitudes of rotation within the base flow vortex cores, and this is evident in Fig. 9. As polymer extensibility L is increased, the peak rotation rate within the developing core located on the lower half of the wake is reduced nearly 60%. This effect, rather than viscoelasticity acting as a perturbation energy sink, is the primary mechanism leading to a stabilization of the two-dimensional viscoelastic wake.

5.2. Mode B stabilization mechanism

To determine how the mode B instability is suppressed, a similar approach was taken to that described above. Fig. 10 shows the components of the energy balance again at $Re = 300$ and various values of L, except at a spanwise wavenumber of $\alpha = 7.6$. At this value of α, the story is quite different. Recall from Fig. 4, the reduction in growth rates as L is increased in this range of α is non-monotonic. Examining Fig. 10, we now find that at $L = 10$, rather than reducing the production of perturbation energy, the production is increased slightly. This, coupled with the presence of the now-positive viscoelastic source (*cf.* Fig. 10), leads to a rise in the instability growth rate. At $L = 20$, however, the production is once again inhibited as it was for lower values of α. This effect is in competition with a strongly destabilizing contribution from the viscoelastic source. At certain times during the shedding period, the viscoelastic contribution is nearly equal in magnitude to that of the production and cannot be neglected from the budget as with the mode A case. The combination of these competing effects at $L = 20$ is an overall decrease in the growth of perturbations – an effect which is even stronger at $L = 30$ (not shown). It thus appears that while the energy production is again begin altered and reduced at high enough L, it is now in competition with a destabilizing effect due directly to viscoelasticity acting on the perturbation. To find the cause of these effects, a Newtonian Floquet analysis was again done on the base flows associated with various values of L. The plots of $|\mu|$ versus time are shown in Fig. 11, comparing the full viscoelastic case to the Newtonian calculation on the viscoelastic base flows. Not surprisingly, changes in the base flow are again directly responsible for the reduction in energy production, seen in the drastic reduction of the values of the Floquet multiplier.

Just as the mode A instability has been associated with an elliptic instability scaling with the primary vortex cores, the mode B instability has been referred to as a "hyperbolic" instability, scaling on the size of the braid region between vortices (see [3,14]). This type of instability originates at the stagnation point within the braid region, surrounded locally by an extensional flow, and is found in other common flows such as shear flows or mixing layers. Unlike the elliptic instability, however, relating the analysis of a simple linear flow field to the full cylinder wake is problematic due to the finite size of the hyperbolic region. Regardless, the linear stability theory of [24] indicates that linear hyperbolic flow (extensional flow) is unconditionally unstable to perturbations – for any flow field, there exists a disturbance wavevector which grows in time. This effect is due to line vortex stretching of the perturbation vorticity near the stagnation point. Furthermore, this instability growth rate scales proportionally with the local principal strain rate, just as the elliptic instability growth rate scaled with local rotation rate. Therefore, in similar fashion to the mode A stabilization mechanism, we find that with increasing polymer extensibility L the strain rate existing between primary vortices in the base flow weakens (as did the rotation rate within a developing core), thus stabilizing the flow. This is seen clearly in Fig. 12.

Unlike the mode A stabilization mechanism, however, is that the same authors also performed linear stability analysis for a viscoelastic extensional flow (see [25]), showing that the same linear flow regime is destabilized in the presence of an Oldroyd-B fluid. This destabilization is manifested in an increased range of unstable spanwise wavenumbers, which is consistent with the destabilizing presence of the viscoelastic perturbation energy source in the mode B case (seen in Fig. 10). What emerges for the high α unstable band is a competition between a base flow-induced stabilization and a viscoelastic perturbation destabilization. At low values of L, the base flow is not modified significantly, and therefore viscoelasticity causes an increase in the observed Floquet multipliers. At higher L, however, the extensional flow within the braid regions of the base flow is weakened enough to decrease the rate of perturbation energy production in a way that ultimately eliminates the growth of all disturbances.

6. Conclusions

A Floquet stability analysis has been performed for viscoelastic flow past a circular cylinder using the FENE-P model. By measuring Floquet multipliers based on computed increases in perturbation energy, we were able to determine the effect that viscoelasticity has on the transitioning cylinder wake. For Newtonian flows, two unstable wavenumber bands have been observed by [4], which are associated with the nonlinear mode A and mode B instabilities found in the cylinder wake at $Re \approx 190$ and $Re \approx 260$, respectively. For the low wavenumber band, viscoelasticity stabilizes the flow and monotonically reduces the growth rate of small spanwise disturbances as the polymer extensibility L is increased. For the high wavenumber band, however, stabilization still occurs but is non-monotonic. For $L = 10$, the growth rates actually increase significantly, while for $L = 20$ and higher, the growth rates are reduced to the point where instabilities will not grow. The linear results were then compared to nonlinear simulations, and general qualitative agreement was found.

To determine what causes this stabilization, the same Floquet analysis was done for Newtonian flow, but using the base flows from the various viscoelastic cases. By doing this, it was shown that the primary mechanism through which viscoelasticity stabilizes the flow is through modification of the underlying base state. Through reductions in vorticity and strain rate in the primary vortices, viscoelasticity reduces the production of disturbance energy and stabilizes the flow for both the mode A and mode B bands of spanwise wavenumber. For mode A, the effect of viscoelasticity on the perturbation is negligible, while for the higher band of wavenumbers, viscoelasticity has a strong destabilizing effect on perturbations. In the case of mode B, the competition between the base state modification and the destabilization of perturbations is then manifested in the non-monotonic reduction of growth rates.

The implications for this work are quite broad. By showing directly that viscoelasticity can achieve wake stabilization, yet another potential application for injection of polymer additives is found. In situations where transition of flow over a bluff body is undesired or its delay is advantageous, polymeric additives may have important applications. Furthermore, what we have shown is that it is merely a change in the base state that is required for stabilization – a condition which does not directly necessitate the use of polymer additives. We speculate that if the recirculation region behind the cylinder can be extended, in addition to weakening and stretching the vorticity of the cores themselves, a desired stabilization can be achieved.

Acknowledgements

The authors would like to acknowledge the Army High Performance Computing Research Center for Agility, Survivability and Informatics, Award No. W911NF-07-2-0027, High Performance Technologies Inc. and Department of the Army (Prime) for partial financial and computational support. In addition, this research has been funded in part by a King Abdullah University of Science and Technology (KAUST) research grant under the KAUST Stanford Academic Excellence Alliance program. Any opinions, findings and conclusions or recommendations expressed in this paper are those of the authors and do not necessarily reflect the views of the KAUST University. Finally, the authors acknowledge the following award for providing computing resources that have contributed to the research results reported within this paper: MRI-R2: Acquisition of a Hybrid CPU/GPU and Visualization Cluster for Multidisciplinary Studies in Transport Physics with Uncertainty Quantification (http://www.nsf.gov/awardsearch/showAward.do?AwardNumber=0960306) This award is funded under the American Recovery and Reinvestment Act of 2009 (Public Law 111-5).

References

[1] D. Richter, G. Iaccarino, E.S.G. Shaqfeh, Simulations of three-dimensional viscoelastic flows past a circular cylinder at moderate Reynolds numbers, Journal of Fluid Mechanics 651 (2010) 415–442.
[2] C.H.K. Williamson, The existence of two stages in the transition to three-dimensionality of a cylinder wake, Physics of Fluids 31 (1988) 3165–3168.
[3] C.H.K. Williamson, Three-dimensional wake transition, Journal of Fluid Mechanics 328 (1996) 345–407.
[4] D. Barkley, R. Henderson, Three-dimensional Floquet stability analysis of the wake of a circular cylinder, Journal of Fluid Mechanics 322 (1996) 215–241.
[5] R. Henderson, Nonlinear dynamics and pattern formation in turbulent wake transition, Journal of Fluid Mechanics 352 (1997) 65–112.
[6] O. Cadot, S. Kumar, Experimental characterization of viscoelastic effects on two- and three-dimensional shear instabilities, Journal of Fluid Mechanics 416 (2000) 151–172.
[7] B. Noack, H. Eckelmann, A global stability analysis of the steady and periodic cylinder wake, Journal of Fluid Mechanics 270 (1994) 297–330.
[8] J. Robichaux, S. Balachandar, S.P. Vanka, Three-dimensional Floquet instability of the wake of square cylinder, Physics of Fluids 11 (1999) 560–578.
[9] S. Camarri, F. Giannetti, Effect of confinement on three-dimensional stability in the wake of a circular cylinder, Journal of Fluid Mechanics 642 (2010) 477–487.
[10] P. Schmid, D. Henningson, Stability and Transition in Shear Flows, 1st edition, Springer, 2001.
[11] H.M. Blackburn, J.M. Lopez, On three-dimensional quasiperiodic Floquet instabilities of two-dimensional bluff body wakes, Physics of Fluids 15 (2003) L57–L60.
[12] C.H.K. Williamson, Vortex dynamics in the cylinder wake, Annual Review of Fluid Mechanics 28 (1996) 477–539.
[13] M.C. Thompson, T. Leweke, C.H.K. Williamson, The physical mechanism of transition in bluff body wakes, Journal of Fluids and Structures 15 (2001) 607–616.
[14] T. Leweke, C.H.K. Williamson, Three-dimensional instabilities in wake transition, European Journal of Mechanics B/Fluids 17 (1998) 571–586.
[15] R.T. Pierrehumbert, Universal short-wave instability of two dimensional eddies in an inviscid fluid, Physical Review Letters 57 (1986) 2157–2159.
[16] B.J. Bayly, Three-dimensional instability of elliptical flow, Physical Review Letters 57 (1986) 2160–2163.
[17] M.J. Landman, P.G. Saffman, The three-dimensional instability of strained vortices in a viscous fluid, Physics of Fluids 38 (1987) 2339–2342.
[18] F. Waleffe, On the three-dimensional instability of strained vortices, Physics of Fluids A 2 (1990) 76–80.
[19] F. Giannetti, S. Camarri, P. Luchini, Structural sensitivity of the secondary instability in the wake of a circular cylinder, Journal of Fluid Mechanics 651 (2010) 319–337.
[20] D. Barkley, Confined three-dimensional stability analysis of the cylinder wake, Physical Review E 71 (2005) 1–3.
[21] S. Kumar, G. Homsy, Direct numerical simulation of hydrodynamic instabilities in two- and three-dimensional viscoelastic free shear layers, Journal of Non-Newtonian Fluid Mechanics 83 (1999) 249–276.
[22] R.R. Lagnado, J.A. Simmen, The three-dimensional instability of elliptical vortices in a viscoelastic fluid, Journal of Non-Newtonian Fluid Mechanics 50 (1993) 29–44.
[23] H. Haj-Hariri, G.M. Homsy, Three-dimensional instability of viscoelastic elliptic vortices, Journal of Fluid Mechanics 353 (1997) 357–381.
[24] R.R. Lagnado, N. Phan-Thien, L.G. Leal, The stability of two-dimensional linear flows, Physics of Fluids 27 (1984) 1094–1101.
[25] R.R. Lagnado, N. Phan-Thien, L.G. Leal, The stability of two-dimensional linear flows of an Oldroyd-type fluid, Journal of Non-Newtonian Fluid Mechanics 18 (1985) 25–59.